Table S1. RT-qPCR primer sequences.

Gene	Sequences
TNF-α	Forward: 5'-CAGGCGGTGCCTATGTCTC-3'
	Reverse: 5'-CGATCACCCCGAAGTTCAGTAG-3'
IL-6	Forward: 5'-CTGCAAGAGACTTCCATCCAG-3'
	Reverse: 5'-AGTGGTATAGACAGGTCTGTTGG-3'
Stat1	Forward: 5'-TCACAGTGGTTCGAGCTTCAG-3'
	Reverse: 5'-GCAAACGAGACATCATAGGCA-3'
Stat2	Forward: 5'-TCCTGCCAATGGACGTTCG-3'
	Reverse: 5'-GTCCCACTGGTTCAGTTGGT-3'
Irf7	Forward: 5'-GAGACTGGCTATTGGGGGAG-3'
	Reverse: 5'-GACCGAAATGCTTCCAGGG-3'
Irf9	Forward: 5'-GCCGAGTGGTGGGTAAGAC-3'
	Reverse: 5'-GCAAAGGCGCTGAACAAAGAG-3'
Ifih1	Forward: 5'-AGATCAACACCTGTGGTAACACC-3'
	Reverse: 5'-CTCTAGGGCCTCCACGAACA-3'
Psmb9	Forward: 5'-CATGAACCGAGATGGCTCTAGT-3'
	Reverse: 5'-TCATCGTAGAATTTTGGCAGCTC-3'
GAPDH	Forward: 5'-AAGCCCATCACCATCTTCCAGGAG-3'
	Reverse: 5'-AGCCCTTCCACAATGCCAAAG-3'

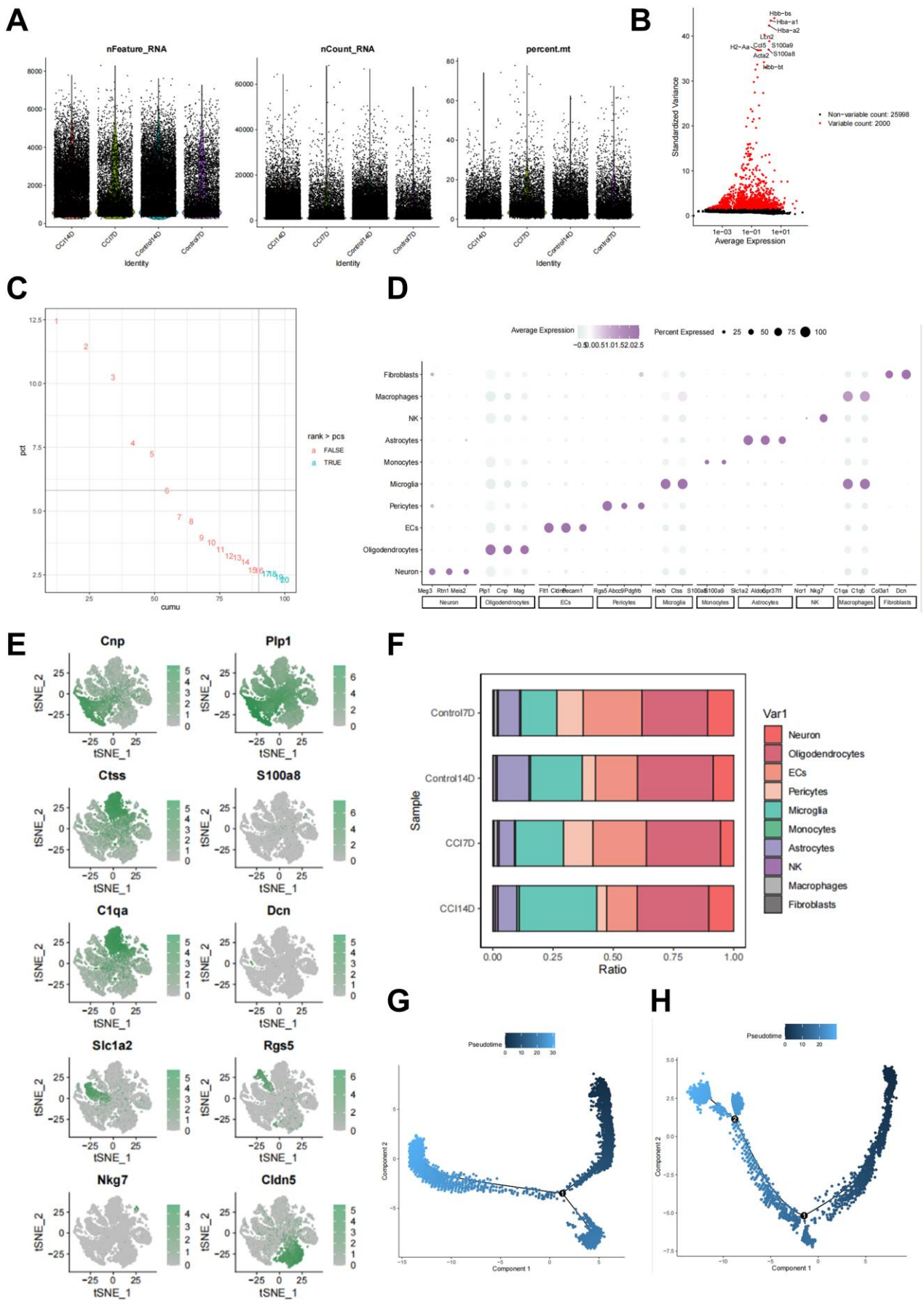

Figure S1. Variable gene and cell component classification in CCI model brain tissue samples

analyzed by scRNA-seq.

Note: (A) Violin plots of gene count per cell (nFeature_RNA), mRNA molecule count (nCount_RNA), and mitochondrial gene percentage (percent.mt) in scRNA-seq data; (B) Variance analysis identifying highly variable genes among 31,053 genes (red dots represent highly variable genes, black dots represent non-variable genes, with the top 10 most variable genes labeled in the plot); (C) The Elbow plot derived from principal component analysis (PCA) was used to determine the number of components to retain based on their individual and cumulative explained variance. Seventeen principal components (PCs) were selected for downstream dimensionality reduction and clustering; (D) Dot plot showing the specific expression genes of primary cell types, with red indicating high expression and blue indicating low expression. The size of the circles represents the percentage of cells expressing the indicated gene; (E) t-SNE plot displaying the expression of marker genes for the primary cell types detected in this study. Green indicates high expression, and gray indicates low expression; (F) Proportion of each cell type in CCI model mice (7D and 14D) and their contralateral standard dorsal spinal tissue samples; (G-H) Trajectory order of microglia (G) and astrocytes (H) subpopulations arranged by pseudotime value. Each dot corresponds to a cell, with darker colors indicating a smaller pseudotime value (closer to the root node). RNA-seq data in this figure derive from GEO: GSE208766 [29].

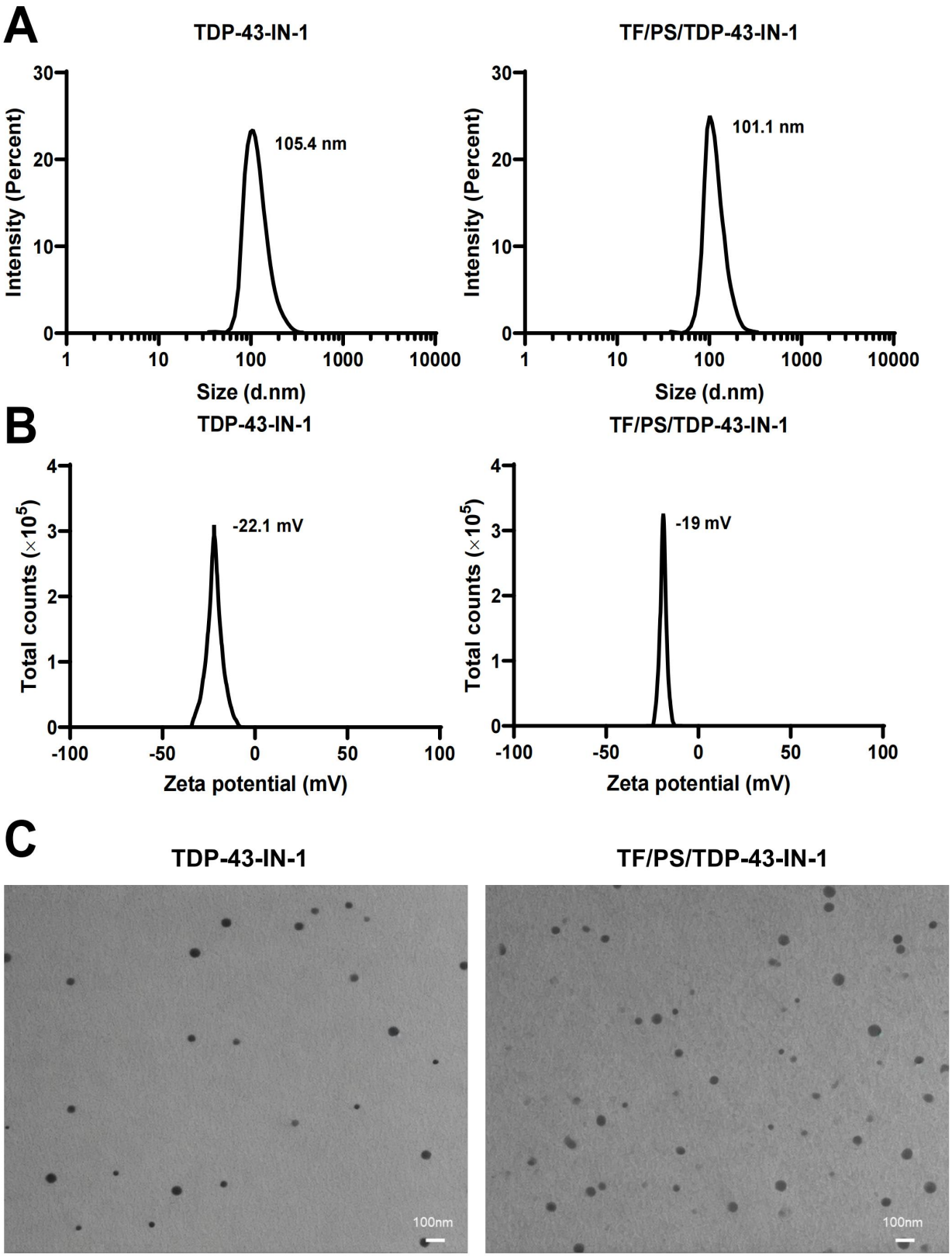

Figure S2. Characteristics of liposomes.

Note: (A) Particle size distribution of TF/PS/TDP-43-IN-1 and TDP-43-IN-1 was assessed to evaluate stability; (B) Zeta potential distribution of TF/PS/TDP-43-IN-1 and TDP-43-IN-1 was measured by dynamic light scattering.; (C) Transmission electron microscopy (TEM) images

confirmed the uniform morphology of TF/PS/TDP-43-IN-1 and TDP-43-IN-1 (scale bar = 100 nm). Cell experiments were repeated three times.

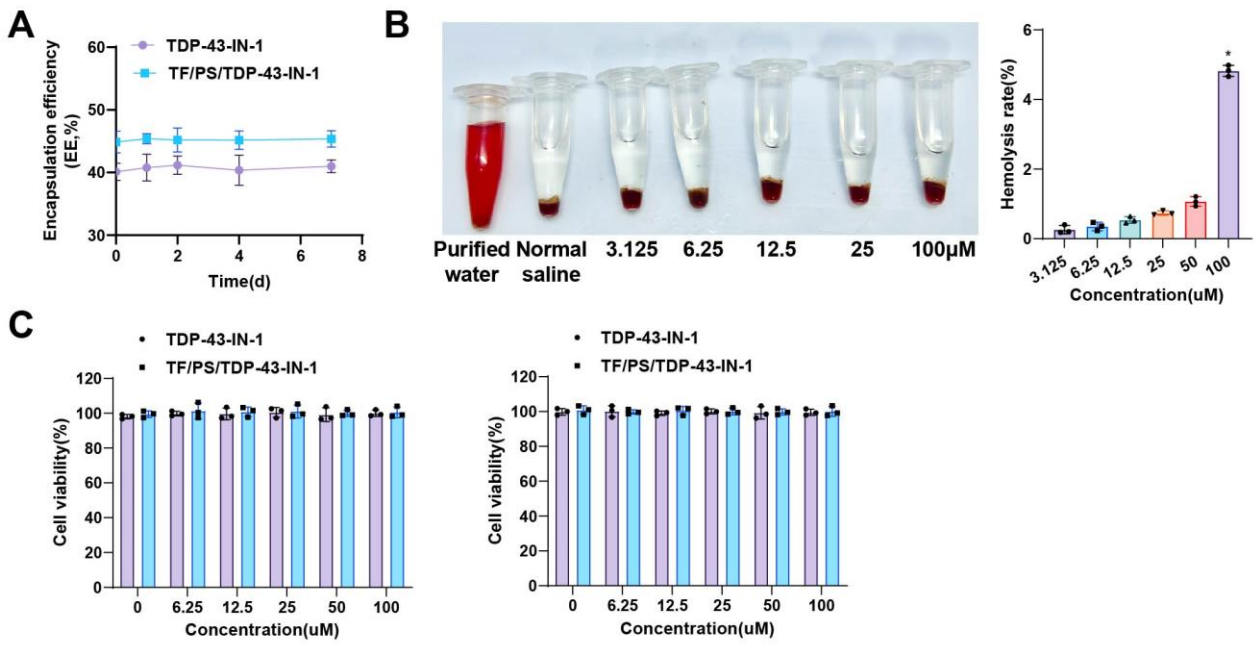

Figure S3. Hemolytic activity of TF/PS/TDP-43-IN-1.

Note: (A) TF/PS/TDP-43-IN-1 and TDP-43-IN-1 exhibited good encapsulation efficiency; (B) Hemolytic activity of TF/PS/TDP-43-IN-1 at various concentrations of TDP-43 (3.125 ~ 100 μM) in a 2% red blood cell solution at 37 ℃. Purified water is defined as 100% hemolysis control, results indicated low cytotoxicity; (C) CCK-8 assays showed that both TDP-43-IN-1 and TF/PS/TDP-43-IN-1 exhibited favorable biocompatibility toward primary astrocytes and microglia *in vitro*. Data conforming to a normal distribution are presented as mean ± standard deviation (SD). Comparisons between two groups were conducted using independent sample t-tests. For comparisons among multiple groups, one-way analysis of variance (ANOVA) was used. * indicates $p < 0.05$ between groups. Cell experiments were repeated three times.

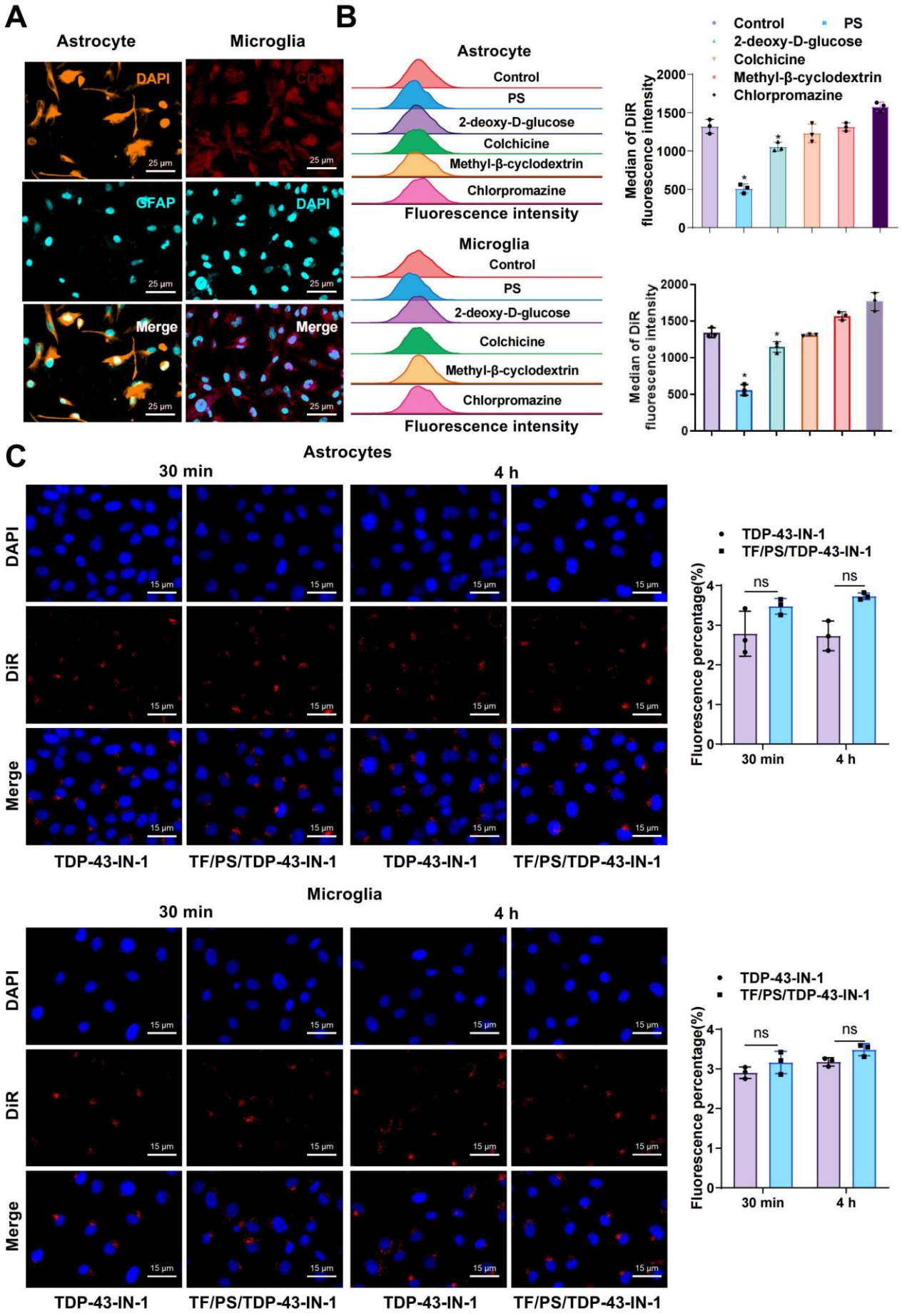

Figure S4. Uptake of liposomes by primary astrocytes and microglia.

Note: (A) Identification of primary astrocytes (GFAP-positive) and microglia (CD68-positive) (scale bar = 25 μm); (B) Mechanism of TF/PS/TDP-43-IN-1 uptake by primary astrocytes and microglia analyzed by flow cytometry; (C) Fluorescence microscopy (scale bar = 15 μm) showed comparable uptake of DiR-labeled TF/PS/TDP-43-IN-1 and TDP-43-IN-1 in non-activated primary astrocytes and microglia, with no significant difference between groups. Data conforming to a normal distribution are presented as mean ± standard deviation (SD). Comparisons between two groups were conducted using independent sample t-tests. For comparisons among multiple groups, one-way analysis of variance (ANOVA) was used. * indicates $p < 0.05$ between groups. ns indicates not significant. Cell experiments were repeated three times.

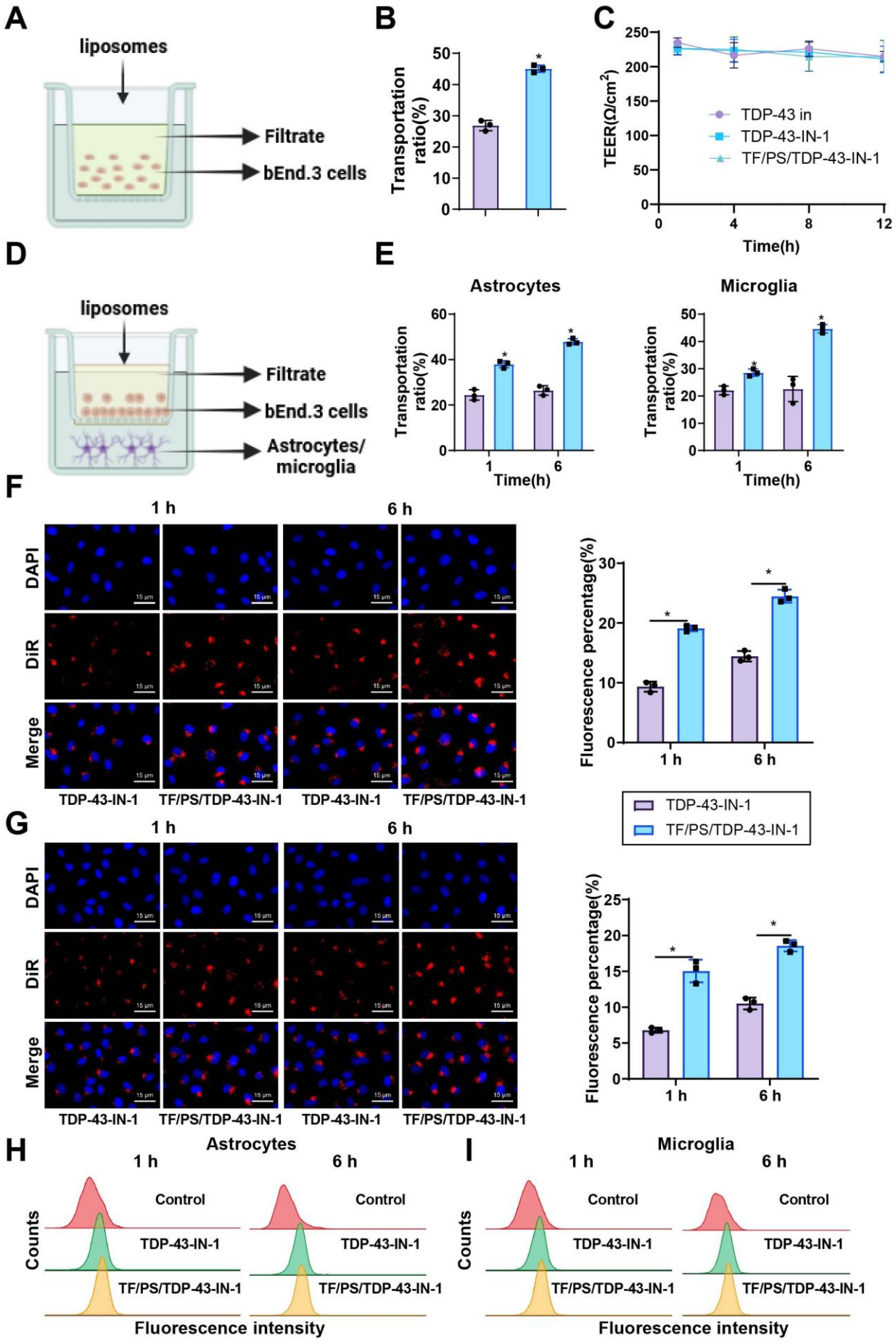

Figure S5. Penetration efficiency of TF/PS/TDP-43-IN-1 across the BBB.

Note: (A) Schematic illustration of the *in vitro* BBB model (Created in BioRender. J, M. (2025) https://BioRender.com/eoy83sa); (B) Statistical graph depicting the translocation of TF/PS/TDP-43-IN-1 across the *in vitro* BBB, indicating good permeability; (C) Comparison of TEER values between donor and receiver chambers confirmed intact barrier integrity; (D) Quantification of BBB penetration efficiency for TF/PS/TDP-43-IN-1 (Created in BioRender. J, M. (2025) https://BioRender.com/mtvgke6); (E) Fluorescence spectrophotometry demonstrated efficient uptake of TDP-43, TDP-43-IN-1, and TF/PS/TDP-43-IN-1 by primary astrocytes and microglia; (F) Fluorescence microscopy (scale bar = 15 μm) showed uptake of nanoparticles by primary astrocytes; (G) Fluorescence microscopy (scale bar = 15 μm) showed uptake of nanoparticles by primary microglia; (H) Flow cytometry revealed efficient internalization of TF/PS/TDP-43-IN-1 and TDP-43-IN-1 by LPS-induced astrocytes; (I) Flow cytometry revealed efficient internalization of TF/PS/TDP-43-IN-1 and TDP-43-IN-1 by LPS-induced microglia. Data conforming to a normal distribution are presented as mean ± standard deviation (SD). Comparisons between two groups were conducted using independent sample t-tests. For comparisons among multiple groups, one-way analysis of variance (ANOVA) was used. * indicates $p < 0.05$ between groups. Cell experiments were repeated three times.

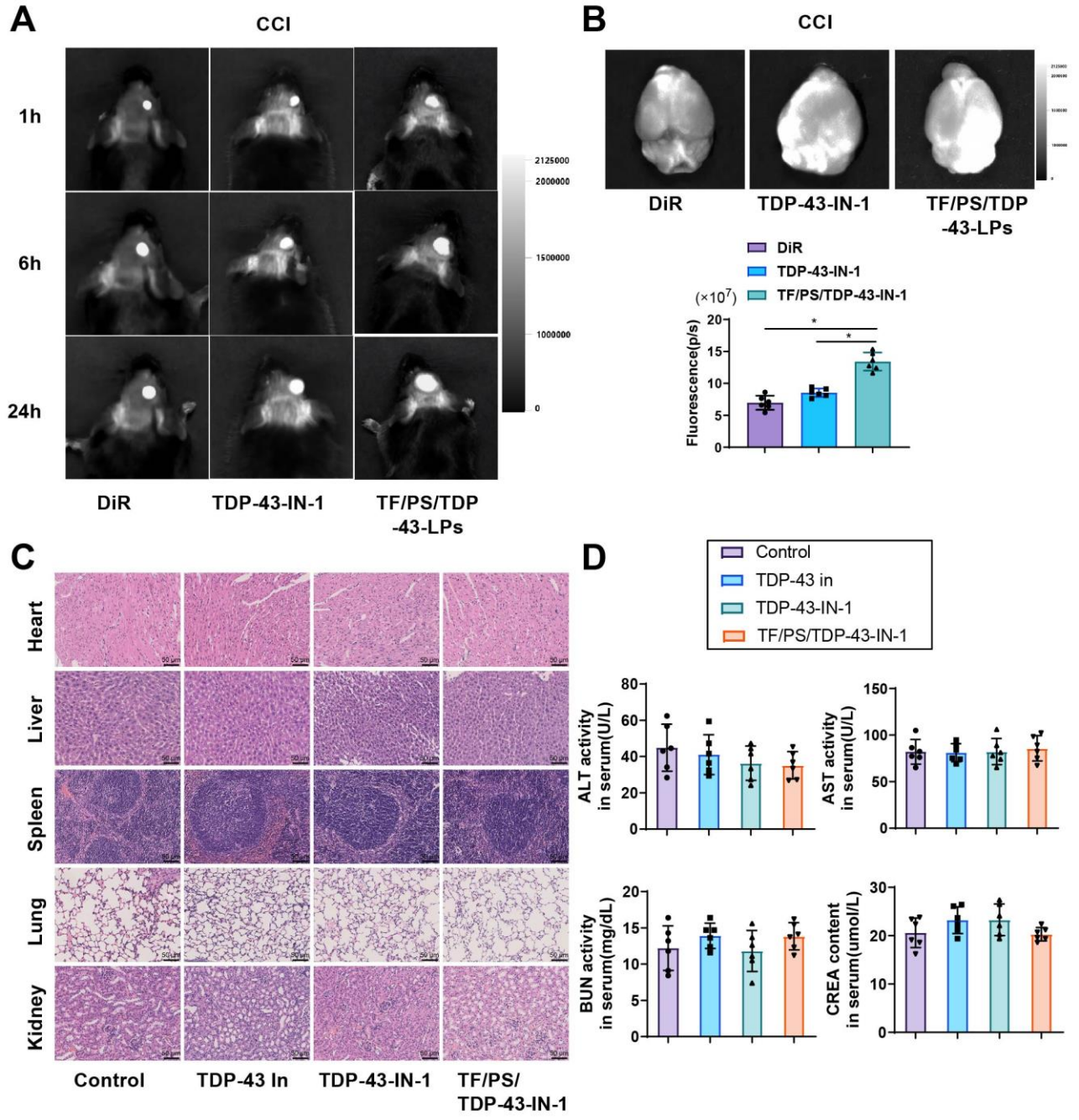

Figure S6. Brain-targeting effects and safety evaluation of liposomes in CCI mice *in vivo*.

Note: (A) Fluorescence analysis of liposome distribution in the brain tissue of CCI mice; (B) Average fluorescence intensity in the brain of CCI mice; (C) H&E staining of brain, heart, liver, spleen, lung, and kidney tissues from CCI mice (scale bar = 50 μm), indicating favorable biosafety.; (D) Statistical comparison of serum ALT, AST, BUN, and CREA levels among TDP-43-in, TDP-43-IN-1, and TF/PS/TDP-43-IN-1 groups in CCI mice indicated good biosafety profiles. Data conforming to a normal distribution are presented as mean ± standard deviation (SD). Comparisons between two groups were conducted using independent sample t-tests. For comparisons among

multiple groups, one-way analysis of variance (ANOVA) was used. * indicates $p < 0.05$ between groups: experimental animals, n=6.

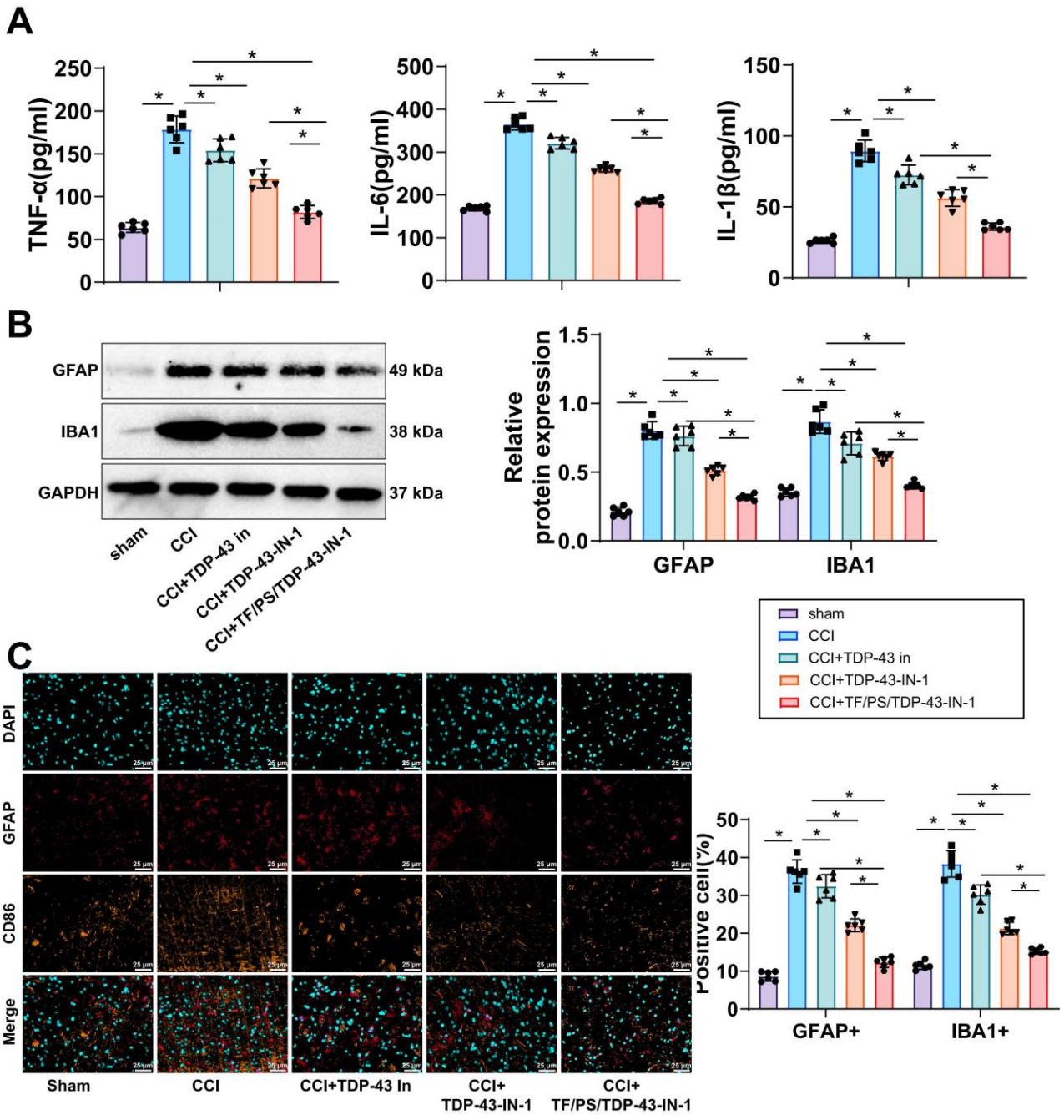

Figure S7. Effects of TF/PS/TDP-43-IN-1 on neuroinflammation.

Note: (A) ELISA assays revealed that serum levels of TNF-α, IL-6, and IL-1β were significantly elevated in CCI mice but markedly reduced after TF/PS/TDP-43-IN-1 treatment; (B) Western blot detection of GFAP and IBA1 expression levels in CCI mice, which was significantly decreased following treatment; (C) Immunofluorescence staining (scale bar = 25 μm) confirmed that GFAP and IBA1 expression was reduced in the spinal cord after TF/PS/TDP-43-IN-1 administration. Data conforming to a normal distribution are presented as mean ± standard deviation (SD). Comparisons between two groups were conducted using independent sample t-tests. For comparisons among

multiple groups, one-way analysis of variance (ANOVA) was used. * indicates $p < 0.05$ between groups: experimental animals, n=6.

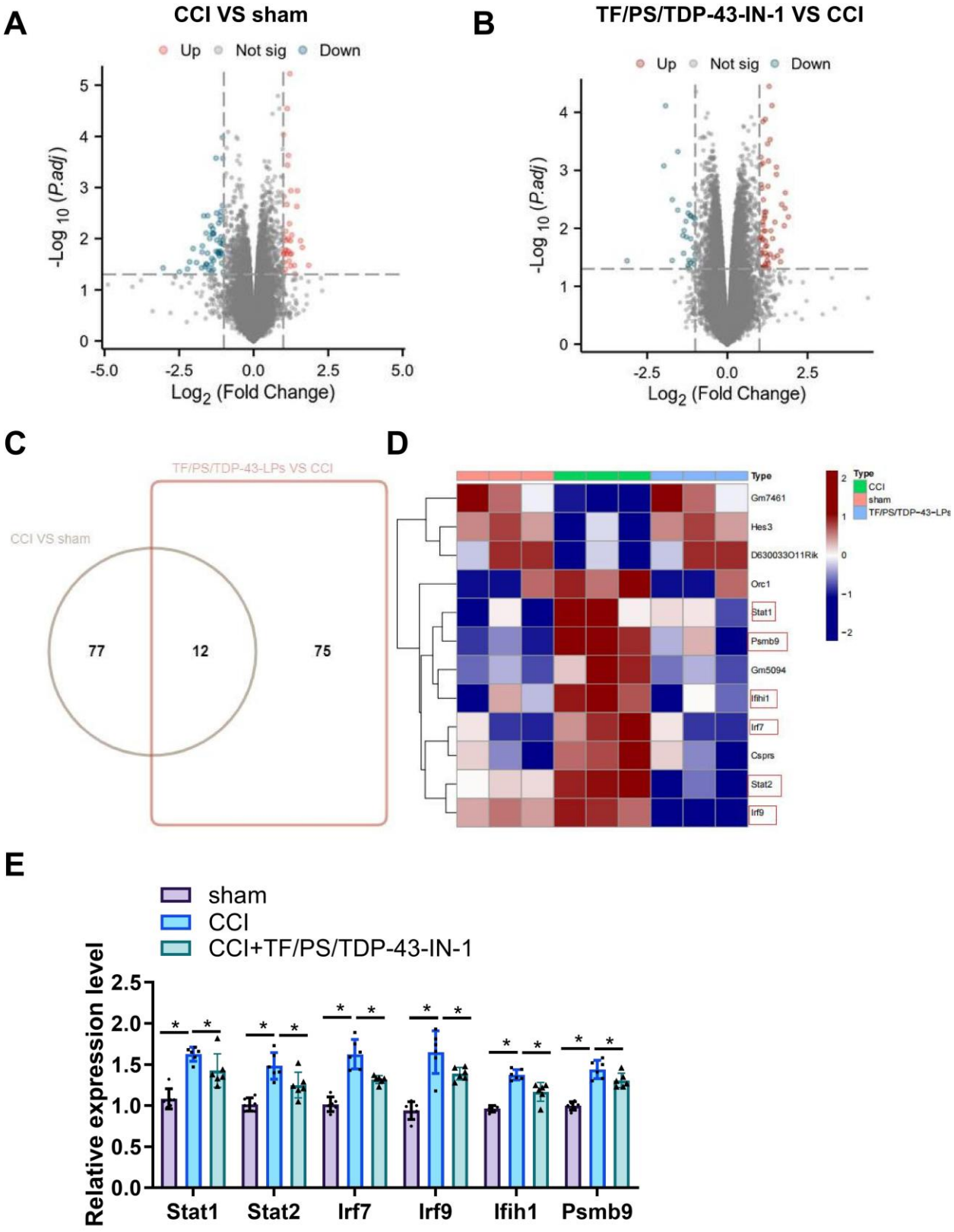

Figure S8. RNA-seq analysis of mice treated with TF/PS/TDP-43-IN-1.

Note: (A–B) Volcano plots display the differentially expressed genes (DEGs). The x-axis represents the $\log_2$ fold change in gene expression, while the y-axis represents the $-\log_{10}$ adjusted P value. Red dots indicate significantly upregulated genes, blue dots indicate significantly downregulated genes,

and gray dots represent non-significant genes. The dashed lines indicate thresholds for significance ($|\log_2 FC| > 1$ and adjusted $P < 0.05$). (A) Comparison of DEGs between CCI model and sham groups (n = 3); (B) Comparison between TF/PS/TDP-43-IN-1–treated and CCI groups (n = 3); (C) Venn diagram showing shared and unique DEGs among groups; (D) Heatmap clustering of representative DEGs across sham, CCI, and treatment groups. Color intensity reflects expression levels from blue (low) to red (high); (E) qRT-PCR detection of type I interferon (IFN)–related gene expression (n = 6). Data conforming to a normal distribution are presented as mean ± standard deviation (SD). Comparisons between two groups were conducted using independent sample t-tests. For comparisons among multiple groups, one-way analysis of variance (ANOVA) was used. * indicates $p < 0.05$ between groups.

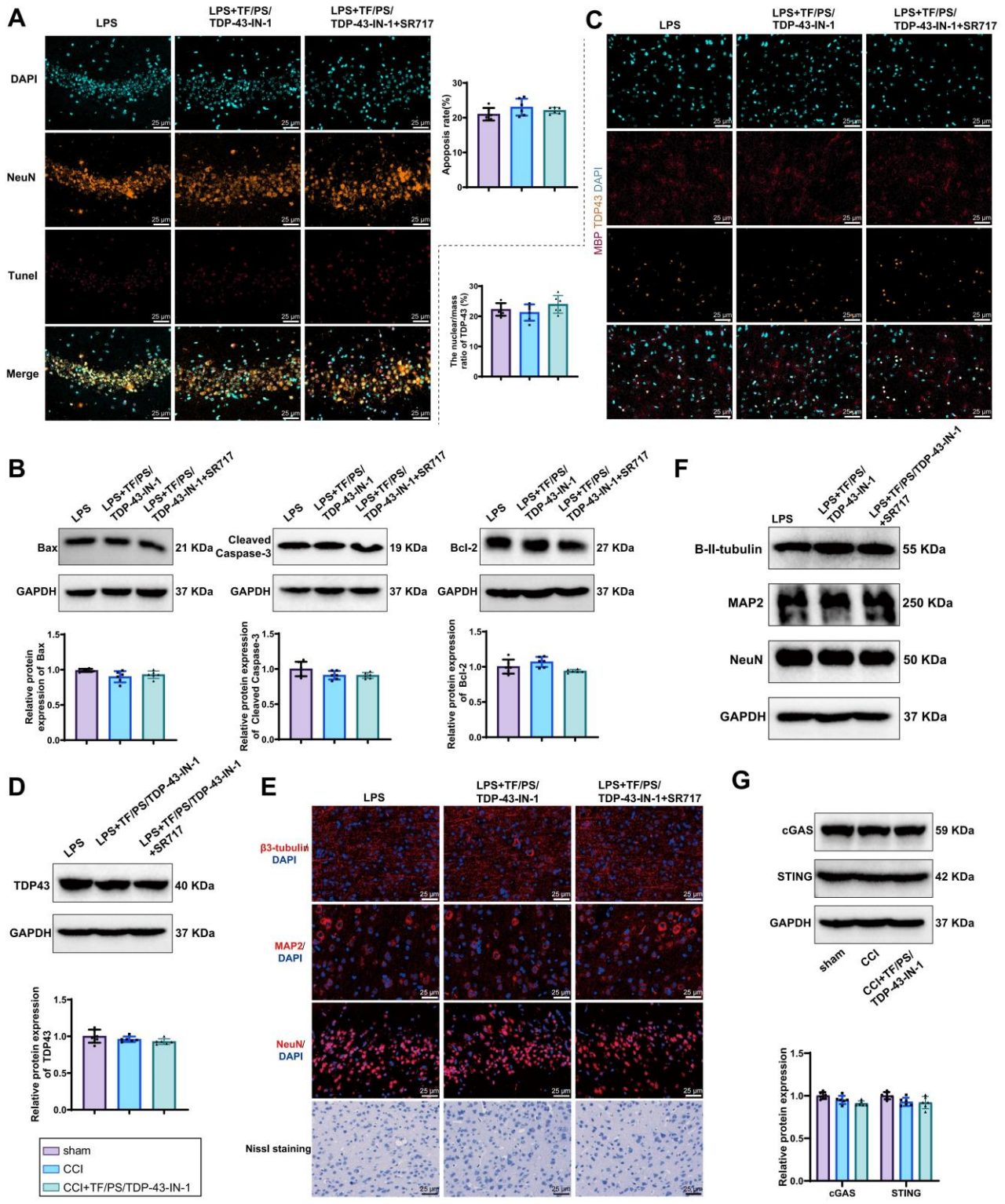

Figure S9. TF/PS/TDP-43-IN-1 Nanoparticles Do Not Alter Neuronal Maturity or Apoptosis

Note:(A) Immunofluorescence staining of NeuN and TUNEL to evaluate neuronal apoptosis; (B) Western blot analysis of Bax, cleaved Caspase-3, and Bcl-2 expression; (C) Immunofluorescence staining of MBP and TDP-43 (scale bar = 25 μm); (D) Western blot analysis of TDP-43 protein levels; (E) Immunofluorescence staining of MAP2, NeuN, β-II-tubulin and Nissl staining (scale bar

= 25 μm); (F) Western blot analysis of MAP2, NeuN, and β-II-tubulin expression; (G) Western blot analysis of cGAS and STING expression in neuronal tissue. Data conforming to a normal distribution are presented as mean ± standard deviation (SD). Comparisons between two groups were conducted using independent sample t-tests. For comparisons among multiple groups, one-way analysis of variance (ANOVA) was used. *$p < 0.05$ compared to CCI group. All cell experiments were performed in triplicate.